

Dislocation-dynamics based crystal plasticity law for the low- and high-temperature deformation regimes of bcc crystal

Ghiath Monnet^{a,*}, Ludovic Vincent^b, Benoit Devincre^c

^a EDF – R&D, MMC, avenue des Renardières, 77818 Moret sur Loing, France

^b CEA, DEN, SRMA, F-91191 Gif-sur-Yvette, France

^c Laboratoire d'étude des microstructures, CNRS-ONERA, 29 avenue de la Division Leclerc, 92322 Châtillon cedex, France

Received 26 January 2013; received in revised form 4 June 2013; accepted 1 July 2013

Available online 29 July 2013

Abstract

Based on recent dislocation dynamics simulations investigations, a set of constitutive equations and model parameters for the description of plasticity of body-centered cubic materials is proposed. Assuming the flow stress to be controlled at low temperatures by the mobility of screw dislocations and by forest interactions at high temperatures, this model allows for the prediction of the mechanical behavior in monotonic loading over a large range of temperatures and strain rates. The consideration of the difference in mobility between screw and non-screw dislocations is found to affect strain hardening in a complex manner. The constitutive equations are implemented in a finite-element method to simulate tensile tests on iron single crystal at different temperatures. The use of finite transformation formalism enables the computation of crystal rotations which affect slip system activities. The calculated critical resolved shear stress and crystal rotations are in good agreement with existing experimental results.

© 2013 Acta Materialia Inc. Published by Elsevier Ltd. All rights reserved.

Keywords: Dislocation; bcc; Crystal plasticity; Thermal activation

1. Introduction

Crystal plasticity modeling at the level of slip systems within finite-element simulations is an important part of continuum mechanics research and has made a great deal of progress since the pioneering work of Pierce et al. [1]. As reviewed by Roters et al. [2], such models are increasingly physically justified. The most important advances are typically: the possibility to account in three dimensions for the real geometrical degrees of freedom associated with dislocation slip systems [3], finite transformation formalism [4], non-local approaches [5,6], the consideration of grain boundary related mechanics [7,8], etc. Hence, a large variety of constitutive equations, called hereinafter crystalline laws (CLs), can be found in the literature. It should be noted that most of these CLs are dedicated to face-centered

cubic (fcc) materials with their well-known slip systems and athermal plastic behavior.

Low-temperature deformation in hexagonal close-packed (hcp) and body-centered cubic (bcc) crystals has specific characteristics such as a large sensitivity to strain rate and temperature [9], a strong difference in dislocation mobility between screw and other dislocation characters [10] and a length dependence of the mobility of screw dislocation segments [11]. This is why specific CLs have been proposed for hcp [12,13] and bcc [14,15] structures. However, the full complexity of the observed plastic properties has not really been addressed. For instance, in the bcc structure the kinetics effects associated with the existence of long screw segments in the dislocation microstructure, as well as the effect of the difference in mobility between different dislocations, are poorly accounted for. In addition, the contribution of non-screw dislocations to strain hardening is usually neglected in the low-temperature regime. As will be seen in this paper, this simplification

* Corresponding author. Tel.: +33 160736473.

E-mail address: ghiathmonnet@yahoo.fr (G. Monnet).

prevents model convergence toward the fcc type of behavior observed with bcc and hcp structures at high temperature, where dislocation mobility no longer controls plastic behavior.

At the same time, several studies based on dislocation dynamics (DD) simulations and dedicated to materials experiencing high lattice friction have been published. They reported on low-temperature deformation in zirconium [16], tantalum [17,18] and iron [19]. These simulations highlighted important features that can now be implemented within more physically based CLs.

We present in this paper a new set of constitutive equations that accounts for a large number of known characteristics of bcc (and hcp) deformation at low temperature. The equations have been deduced from recent DD simulation results [20], which allowed for an accurate description of the collective behavior of large dislocation densities in iron at low [19] and high [21] temperatures. The CL solutions evolve with temperature and therefore provide a detailed description of plastic properties from relatively low temperatures towards the athermal regime. The paper is organized as follows. In the next section we describe the flow equation connecting the shear strain rate on a given slip system to the applied shear stress on this system. Then we introduce and describe the state variables in connection with the microstructure parameters. In Section 4, we present the stress decomposition needed to determine the effective stress on screw segments, known to control the yield stress at low temperature. In Section 5, the storage-recovery equations that model the evolution of dislocation densities with deformation are presented. In Section 6, we present finite-element (FE) simulations of two tensile test geometries using the proposed CL. The last section is dedicated to a discussion and concluding remarks.

2. The flow equation

2.1. Plastic flow at high temperature

At sufficiently high temperature and mesoscopic scale, the free-flight motion of dislocation segments is well described by an athermal viscous velocity law $v = (b/B) \tau_{eff}$, where B is the viscous coefficient, b is the magnitude of the dislocation Burgers vector and τ_{eff} is the effective stress on the segment. However, the flow stress at the macroscopic level is known to contain a small thermal component [22–24] responsible for the dependency of flow stress on strain rate. The origin of this thermal component can be attributed to the thermally activated jog drag or destruction of cross-states in the dislocation microstructure. For this reason, the high-temperature regime is referred to hereinafter as the “drag regime”. The Orowan relation implies that the effective steady velocity of dislocations is thermally activated with characteristically large activation volumes [23,24]. This allows for the simplification of the Arrhenius equation in the form of a power law, widely used in the

literature (e.g. [25,26]). The shear strain rate on a slip system “ s ” in the drag regime can then be given in the form:

$$\dot{\gamma}_{drag}^s = \dot{\gamma}_o \left[\frac{|\tau_{app}^s|}{\tau_c^s} \right]^n \text{sign}(\tau^s), \quad (1)$$

where $\dot{\gamma}_o$ and n are constant, τ_c^s is the critical stress and τ_{app}^s is the resolved shear stress on system s . In the following a superscript, say s , denotes the number of the slip system of interest, while the subscripts refer to the nature of the variable. The critical stress is given here by a Taylor-like equation [27]:

$$\tau_c^s = \tau_f^s + \sqrt{\sum_{i=1}^N a^{si} \rho^i}, \quad (2)$$

where τ_f^s is the alloy friction, ρ^i is the dislocation density of an obstacle system i (with N the total number of obstacle systems) and a^{si} are the interaction coefficients with obstacle system i . Recently, interaction coefficients between slip systems were calculated for bcc materials with the help of DD simulations [21,28].

2.2. Plastic flow at low temperature

In bcc crystals, the early stage of plastic deformation (stage 0) is known to play an important role in plastic flow in the low-temperature regime, where lattice friction strongly restricts screw dislocation mobility [29,30]. Stage 0 is characterized by an anelastic behavior associated with the motion of non-screw dislocations at low stresses and leads to a strong increase in the density of screw dislocations. However, modeling of stage 0 is complex and requires considering different constitutive laws for the screw and non-screw dislocation populations [13]. For this reason, stage 0 was disregarded in the present model. Rather, we consider the initial microstructure to be that obtained at the end of stage 0, i.e. at the onset of the irreversible plastic flow [29] associated with the motion of screw dislocations. In other words, we consider the mobile dislocation density to be saturated at the end of stage 0. As DD simulation results [16,19] confirmed that the flow stress at low temperature is controlled by the effective stress on screw dislocations, regardless of the mobility law assigned to non-screw dislocations, we term this regime the “friction regime”. The effective stress is the stress necessary to produce a velocity v^s of screw dislocation segments. This velocity can be expressed as a function of the temperature and the effective stress [31,32]. Several solutions were found for DD simulations of Ta [33], Zr [34] and Ti [13]. For iron, Naamane et al. [19] proposed the expression:

$$v^s = H_l^s \exp \left(- \frac{\Delta G(\tau_{eff}^s)}{kT} \right) \text{sign}(\tau_{eff}^s), \quad (3)$$

where H is a frequency factor [17] connected to the Debye frequency ν_D by $H = \nu_D b / l_{dk}$, where l_{dk} is a characteristic length of the double-kink mechanism, close to $10b$. H is

considered as a constant parameter in our model. In Eq. (3), l_s^s is the average length of the screw dislocation segments, k is the Boltzmann constant and T is the absolute temperature. An interesting feature of Eq. (3) is that the velocity of the segment is proportional to its length, as recently confirmed experimentally in iron [35]. ΔG is the activation energy for double-kink nucleation under a given effective resolved shear stress. In the case of iron, direct analysis of experimental loading curves [19] provided the following expression that was found to cover the entire stress range observed in the thermal regime:

$$\Delta G(\tau_{eff}^s) = \Delta G_o \left(1 - \sqrt{\frac{\tau_{eff}^s}{\tau_o}} \right), \quad (4)$$

where ΔG_o and τ_o are two fitting parameters. The square-root dependency in Eq. (4) is in agreement with simple theoretical approaches [36,37] and experimental results [38], and was recently confirmed with atomistic simulations [39]. In order to express the shear rate, use is made of the Orowan relation including screw and non-screw dislocations: $\dot{\gamma}_{friction}^s = \rho_{sc}^s b^s v_{sc}^s + \rho_{ed}^s b^s v_{ed}^s$, where the subscripts “sc” and “ed” denote here the screw and non-screw characters, respectively. Although non-screw dislocations do not control the flow stress, their contribution to plastic shear cannot be neglected. Their density is very low compared to that of screw dislocations, but their velocity is very large [13]. As suggested by Louchet et al. [40] and confirmed later by DD simulations [18], apart from stage 0, the contribution of non-screw dislocations to plastic shear is equal to that of screw dislocations. The shear rate equation can thus be simplified and takes the form $\dot{\gamma}_{friction}^s = 2\rho_{sc}^s b^s v_{sc}^s$. Moreover, since the microstructure at the end of stage 0 is mostly formed of screw dislocations, we approximate the mobile screw dislocation density by the initial density, which also corresponds to the mobile density ρ_m^s at the onset of stage I. Considering all these features, we deduce the flow equation for slip system s :

$$\dot{\gamma}_{friction}^s = 2\rho_m^s b H l_s^s \exp \left(-\frac{\Delta G_o}{kT} \left(1 - \sqrt{\frac{\tau_{eff}^s}{\tau_o}} \right) \right) \text{sign}(\tau^s). \quad (5)$$

The strain rate in the friction regime is thus proportional to the average length of screw dislocations. This feature has not always been taken into account in the literature [12,41].

As the mobile dislocation density is supposed to saturate at the end of stage 0, ρ_m^s is constant in our model. From Eq. (5), we see that the shear velocity varies exponentially with the temperature and the square root of the effective stress. In the following section, we see how these parameters vary during deformation as a function of the microstructure parameters.

2.3. General flow equation

At intermediate temperatures, the flow stress can be controlled by both drag and friction mechanisms. A rule

of mixture must be adopted in order to account for these two mechanisms. Let us consider the following reasoning. Considering both mechanisms are independent of each other, they must act concurrently and their slowing effects add. The time increment Δt necessary for dislocations to sweep a given area is thus the sum of the time increment Δt_{drag} necessary to move the dislocation whose mobility is only controlled by jog drag and the time increment $\Delta t_{friction}$ necessary to move the jog-free screw dislocation moving by nucleation and migration of kink-pairs. At a given effective stress, Δt_{drag} and $\Delta t_{friction}$ are respectively proportional to the inverse of $\dot{\gamma}_{drag}^s$ and $\dot{\gamma}_{friction}^s$. Since Δt is also proportional to the inverse of the total strain rate, we deduce:

$$\frac{1}{\dot{\gamma}^s} = \frac{1}{\dot{\gamma}_{drag}^s} + \frac{1}{\dot{\gamma}_{friction}^s}. \quad (6)$$

The total strain rate is thus the harmonic mean of the strain rates associated with individual mechanisms. Fixing a total strain rate, Eq. (6) implies that the effective stress must be increased in order to enable each mechanism to provide at least one-half of the imposed strain rate. Two asymptotic behaviors can be predicted from Eq. (6). At low temperature and high effective stress, $\dot{\gamma}_{drag}^s$ is much larger than $\dot{\gamma}_{friction}^s$ and the total strain rate becomes close to $\dot{\gamma}_{friction}^s$, i.e. plastic flow is controlled by lattice friction. At high temperature and low effective stress, $\dot{\gamma}_{drag}^s$ is smaller than $\dot{\gamma}_{friction}^s$ and plasticity becomes controlled by drag mechanisms. Hence, Eq. (6) allows for a smooth transition from the low-temperature to the high-temperature deformation regimes.

3. State variables

3.1. Non-screw dislocation curvature in the friction regime

For the sake of simplicity we assume that the mobility of edge dislocations is much higher than that of screw dislocations in the friction regime and that the effective stress on edge dislocations is negligibly small compared with that on screw segments. Experiments [11] and DD simulations of iron plasticity at low temperatures [20] have shown that when a moving screw dislocation encounters an obstacle, two non-screw sections are formed in the vicinity of the obstacle, leading to a decrease of the average length of screw dislocations (see Fig. 1).

Since the moving dislocation is submitted to a given effective stress, the non-screw section experiences a curvature of radius R^s . Using a simple line tension model, this curvature radius equals roughly $R^s = \mu b / (2\tau_{eff}^s)$, where μ is the shear modulus. As illustrated in Fig. 1, the obstacle can be bypassed in two conceptually different ways [20]. (i) When the obstacle spacing λ^s is sufficiently large (Fig. 1a), the continuous motion of the screw section induces the rotation of the non-screw sections around the obstacle until the breaking angle θ is reached under the same curvature radius R^s . By virtue of Eq. (5), the effective

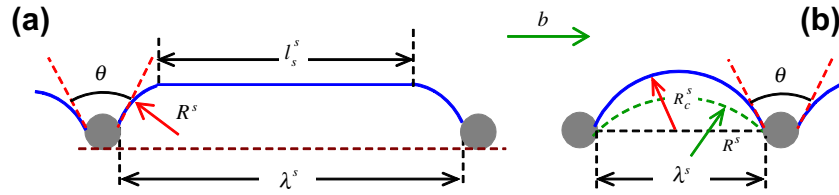


Fig. 1. Schematic drawing of the two existing critical configurations for screw dislocations bypassing obstacles at low temperatures: (a) large spacing configuration; (b) small spacing configuration. The detailed nature of the obstacles is not represented. Rather, only the average size of the obstacle is shown with a simple radius of the contact reaction.

stress must in that case be logarithmically increased in order to balance the decrease of the screw segment length with no contribution of the dislocation line tension. (ii) When the obstacle spacing λ^s is small (Fig. 1b), the motion of the pinned dislocation leads to the reduction of the screw segment length down to the critical value l_c of the kink-pair length. Then, if the breaking angle is not yet reached, the stress must be further increased in order to overcome the dislocation line tension and decrease the curvature radius down to the critical value R_c^s , which induces a line tension resistance as will be seen in Section 4. In all what follows we will distinguish the two cases in (i) and (ii) as the large and low spacing cases, respectively.

3.2. Dislocation obstacle strengthening

The strengthening induced by obstacles cutting the dislocation glide planes is now investigated. For the large spacing case (Fig. 1a), the obstacle strength affects only the length of the straight screw segment. However, in the case of the small spacing regime (see Fig. 1b), when obstacles are of infinite resistance, the critical bypassing angle θ (see Fig. 1) is zero and the critical curvature radius corresponds to $R_c^s = \lambda/2$. For weaker obstacles, R_c^s is larger and can be approximated by $\lambda/(2\cos(\theta/2))$. The mean obstacle strength can then be defined as $\alpha^s = \cos(\theta/2)$, which leads to:

$$R_c^s = \frac{\lambda^s}{2\alpha^s}. \quad (7)$$

When the microstructure contains different types of obstacles (e.g. forest obstacle, particles, irradiation defects) with their respective densities ρ^j and specific strengths, DD simulations [21] have shown that the average obstacle strength follows a quadratic average rule and can be accurately evaluated using the formula:

$$\alpha^s = \sqrt{\sum_{j \neq s} a^{sj} \frac{\rho^j}{\rho_{obs}^s}}, \quad (8)$$

where ρ_{obs}^s is the sum of obstacle densities for system s and a^{sj} is the interaction coefficient between the mobile system s and the obstacle family j . In the above equation a logarithmic term related to dislocation line energy [21,42] has been neglected for reasons of simplicity. Furthermore, it can be noted that when the obstacle densities are close to each

other, α^s is identical for all slip systems and can be approximated by the square root of the average of interaction coefficients: $\alpha^s = \sqrt{\langle a^{sj} \rangle}$. Hence, in the case of forest dislocations, α^s recovers its expected value of 0.3. The main virtue of Eq. (8) is the possibility to account for additional obstacles such as small particles, voids, etc. [42].

3.3. Interaction statistics

As shown in Fig. 1, the average length l^s of screw segments depends on the average obstacle spacing λ^s . It is therefore important to correctly evaluate the length λ^s . When the dislocation mobility is isotropic (drag regime), the probability density $p(r)$ of finding an obstacle at a distance r obeys a 2-D Poisson's distribution: $p(r) = 2\pi\rho_{obs}^s r \cdot \exp(-\rho_{obs}^s r^2)$, as suggested by Kocks [43] and Cuitino and Ortiz [44]. The average planar spacing is thus equal to the square root of the average area per obstacle A (see Fig. 2a). This assumption lies at the heart of many constitutive relations for crystalline plasticity and leads to the well-known $\sqrt{\rho_{obs}^s}$ proportionality of the forest strength. Therefore, we have:

$$\lambda_{drag}^s = \frac{1}{\sqrt{\rho_{obs}^s}}. \quad (9)$$

However, when the dislocation mobility is anisotropic, such as in the friction regime, the 2-D Poisson distribution of interaction statistics does not apply and DD simulations [20] have confirmed that the correct interaction statistics is different.

Stainier et al. [14] proposed a probability density of obstacles along the Burgers vector direction: $p(l) = \sqrt{\rho_{obs}^s} \exp(-\pi\rho_{obs}^s l^2)$. The average obstacle spacing obtained with this distribution is:

$$\lambda_{friction}^s = \int \sqrt{\rho_{obs}^s} \exp(-\pi\rho_{obs}^s l^2) dl = \frac{1}{2\pi\sqrt{\rho_{obs}^s}}, \quad (10)$$

which is surprisingly lower than the average planar spacing in the drag regime, given by Eq. (9). This feature is in contradiction with DD simulation results [20], where the spacing is always found to be much larger than that in the drag regime. More realistically, Alankar et al. [13], in a work dedicated to the transition between stage 0 and 1 (noted stage 1 and 2 by the authors), defined $\lambda_{friction}^s$ as simply equal to $20 \times \lambda_{drag}^s$, with no further justification. For the

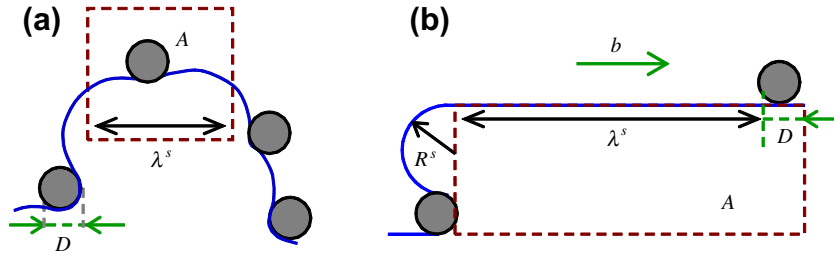


Fig. 2. Interaction statistics with (a) an isotropic flexible dislocation line and (b) a straight dislocation submitted to large lattice friction on its screw section.

present model, a simple statistical approach based on geometrical arguments already used by several authors [45,46] is revisited. In the friction regime, screw dislocations can be considered as straight and must advance a distance X to unpin from an obstacle. Although the initial picture does not account for non-screw dislocation curvature, this description can be used as the starting point to define a probability distribution that has been confirmed by DD simulations [20]. Consider a dislocation segment pinned at both ends with two obstacles (Fig. 2b). The left arm has to move forward a distance $X = 2R^s + D$ in order to unpin, where D can be the particle size or a junction length. We look for the probability of finding an obstacle within a ribbon of width X and length between λ^s and $\lambda^s + d\lambda^s$. Since the distribution of obstacles is random with a constant surface density ρ_{obs}^s , this distribution is 1-D Poissonian [47,48] with λ^s as a random variable and $X\rho_{obs}^s$ as linear density. The probability density is thus $p(\lambda^s) = X\rho_{obs}^s \exp(-X\rho_{obs}^s \lambda^s)$. The corresponding average value for λ^s , the obstacle spacing in the friction regime, is:

$$\lambda_{friction}^s = \int_0^\infty X\rho_{obs}^s \lambda \exp(-X\rho_{obs}^s \lambda) d\lambda = \frac{1}{X\rho_{obs}^s}. \quad (11)$$

Since X at low temperatures is much lower than $(\rho_{obs}^s)^{-0.5}$, $\lambda_{friction}^s$ is then much larger than λ_{drag}^s . At intermediate temperatures, when approaching the drag regime, R^s increases and $\lambda_{friction}^s$ converges to λ_{drag}^s . Eq. (11) no longer applies. To continuously pass from one regime to another, we propose the following general expression:

$$\lambda^s = \frac{1}{\min(\sqrt{\rho_{obs}^s}; X\rho_{obs}^s)} - D. \quad (12)$$

Knowing the average spacing of obstacles, the average length of screw segments can be taken equal to $\lambda^s - 2\alpha^s R^s$. One should notice that the obstacle strength and size (α^s and D , respectively) directly affect the screw dislocation length. Also, as may be intuitive, l_s^s tends to zero when R^s increases or λ^s decreases. However, in order to avoid singularity, we impose in the model that l_s^s cannot be less than the critical length of kink-pairs l_c , and therefore:

$$l_s^s = \max\{\lambda^s - 2\alpha^s R^s; l_c\}. \quad (13)$$

In addition, in agreement with existing theories of kink-pair nucleation [36,37], we suppose that the critical width of kink-pairs is stress dependent. In order to account for this feature, we recall that l_c intervenes in the definition

of the activation volume V of the kink-pair nucleation process: $V = l_c b^2$. We propose to fit l_c on experimental curves measuring the activation volume variations as a function of the effective stress [49–51]. In our simulations, it is more convenient to fit V to the temperature. Since most experimental measurements are carried out at similar strain rates (close to 10^{-4} s^{-1}), we consider experimental values of V to be connected with temperature via the dependency of the effective stress on the temperature. The result of such fitting with a second-order polynomial gives:

$$l_c = 300 \left(\frac{T}{T_o} \right)^2 b. \quad (14)$$

Eq. (14) is a simple equation catching important features of l_c . Hence, l_c goes to zero with decreasing temperature (increasing effective stress) and diverges at high temperature (low effective stress), which is essentially the behavior observed in experiments.

4. Stress decomposition

The only driving force for plastic deformation considered in the present model is the applied shear stress. By definition other shear stress components are taken as absolute values and constitute resistance to the plastic flow. The effective shear stress on system s is decomposed into:

$$\tau_{eff}^s = |\tau_{app}^s| - \tau_c^s,$$

with

$$\tau_c^s = \sqrt{\tau_{self}^s{}^2 + \tau_{LT}^s{}^2} + \tau_f^s, \quad (15)$$

where τ_c^s is the critical stress and τ_{self}^s the stress interaction between all dislocations belonging to the same slip system. It should be noted here that in the present model, the self-stress definition is different from the usual quantity used in dislocation theory and designates the stress induced by one dislocation on itself. In Eq. (15), τ_{LT}^s is the line tension resistance and τ_f^s the alloy friction stress resulting from solid solution effects. The quadratic superposition rule used in Eq. (15) is identical to that leading to the Taylor decomposition in Eq. (2). The applied stress is easy to compute from the external stress tensor. However, the alloy friction stress related to solid solution is somehow difficult to assess at low temperature. The formulation adopted in Eq. (15) implies a linear superposition with the lattice friction, responsible for the effective stress. This feature is neither supported by

experiment nor by atomistic simulations. In experiments, some authors reported a transition between solid-solution hardening at low temperatures to softening at intermediate temperatures [51]. Others reported only softening [52,53], whereas others reported only hardening [54]. On the one hand, there is no evidence that lattice friction on screw dislocations increases in alloys, and, on the other hand, if this strengthening can be proved, there is no reason why this source needs to be linearly added to the lattice friction of pure bcc metals. In all cases, the reported effect of solid solution is rather weak. For these reasons, we consider in this paper that solid-solution strengthening is neglected, i.e. $\tau_f^s = 0$.

Dislocations of the same slip system s gliding on different planes experience elastic dipolar attractions [21] independent of the temperature regime. As the average spacing of these dislocations scales with $1/\sqrt{\rho^s}$ [55], dipolar interaction obeys the same rules as forest interaction. Hence:

$$\tau_{self}^s = \mu b \sqrt{a_{self} \rho^s}, \quad (16)$$

with a_{self} is the self-interaction coefficient. Here we can note that dipolar interactions are also possible with the two collinear systems of the bcc structure, due to the equivalent geometry. However, during deformation, the interaction with the collinear systems may lead to contact and annihilation reactions, while the self-interaction, defined in Eq. (16), represents only long-range interactions involving dislocations moving on parallel planes, with no contact or intersections. This is why interactions with the collinear systems are not included in Eq. (16), but only as a forest mechanism.

Calculation of the stress resistance associated with the line tension component in Eq. (15) is less obvious and requires a more detailed justification. In contrast with the assumption made in some CLs [46], DD simulations [20] have shown that the line tension component is not always present. As illustrated in Fig. 1, when the obstacle spacing is large, dislocations can move between obstacles, keeping long straight sections of screw character, evidencing that the dislocation mobility is not affected by line tension effects. Consequently as long as $l_s^s > l_c$, the line tension contribution to the effective stress is zero.

Alternatively, when the obstacle spacing is low and $l_s^s = l_c$, dislocation unpinning requires an increase in dislocation curvature between obstacles, which generates a line tension resistance (Fig. 1b). The latter derives from the mechanical work necessary to decrease the radius of curvature from $R^s = \mu b / (2\tau_{eff}^s)$ to $R_c^s = l_c / (2\alpha^s)$. As the stress necessary to achieve a curvature R_c^s is roughly $\mu b / (2R_c^s)$, τ_{TL}^s can be given by [20]:

$$\tau_{TL}^s = \alpha^s \mu b \left(\frac{1}{\lambda^s} - \frac{1}{2\alpha^s R^s + l_c} \right). \quad (17)$$

Note that l_c is added to $2\alpha^s R^s$ in the last term of Eq. (17) to ensure solution continuity with the large obstacle spacing solution in Eq. (13). As expected, at high temperatures Eq. (17) tends to the well-known Taylor equation and Eq. (15) tends to Eq. (2).

5. Dislocation density rate equation

Modeling dislocation density variation is one of the most tedious problems of crystal plasticity. Alankar et al. [13] proposed a density rate equation dedicated to the friction regime. In this model, multiplication and annihilation are related to the velocity of both edge and screw dislocations. This approach is not appropriate in the present work since it does not aim at modeling stage 0. Although other solutions are reported in the literature [8,56], we decided for reasons of simplicity to adapt the classical storage-recovery equation [57] to the specificity of the friction regime.

The storage-recovery scheme gives explicitly the evolution of the dislocation density on system s as a function of the shear rate on the same system in the form:

$$\frac{\dot{\rho}^s}{|\dot{\gamma}^s|} = \frac{1}{b} \left[\frac{1}{\Lambda^s} - y^s \rho^s \right], \quad (18)$$

with y^s a material parameter that accounts for dynamic recovery and Λ^s the harmonic average of dislocation mean free paths that account for the different dislocation storage processes taking place during plastic slip:

$$\frac{1}{\Lambda^s} = \frac{\sqrt{a_{self} \rho^s}}{K_{self}} + \frac{\alpha^s \sqrt{\rho_{obs}^s}}{K_{obs}}. \quad (19)$$

In Eq. (19), K_{self} and K_{obs} are two mean free path coefficients, linked to the self-interaction and forest interaction, respectively [58].

The storage-recovery formalism is in principle dedicated to the drag regime in which the effective stress is negligible in comparison with the critical stress. In such conditions, Λ^s is proportional to the average spacing and strength of the obstacles. As we have seen in the previous section, the strengthening mechanisms do not scale with the average obstacle spacing in the friction regime. This is why the following modifications are proposed.

First, the values of the interaction coefficients calculated with DD simulations [21,28] can be used to evaluate the local pinning force of obstacles (e.g. Eq. (8)) but not as a measure of the self or forest strength, as implicitly assumed in Eq. (19). This is because the stress decomposition according to the Taylor equation (Eq. (2)) does not apply in the friction regime. In order to account for the evolution of obstacle strength with temperature, we consider the effect of the lattice friction, i.e. τ_{eff}^s , on the interaction coefficients to be equivalent to the effect of solid-solution strengthening on junction strengths observed with DD simulations [59]. In these simulations, it was shown that α^s decreases strongly and linearly with τ_{eff}^s . Consequently, we propose in the present model that a^{ij} is a quadratic function of τ_{eff}^s . The corrected coefficients are then called “effective” and can be given by the expression:

$$a_{eff}^{ij} = a^{ij} \left(1 - \frac{\tau_{eff}^s}{\tau_o} \right)^2. \quad (20)$$

Second, since the interaction statistics with obstacles is modified in the friction regime, the contribution to dislocation storage coming from forest interactions must be modified. K_{obs} represents the mean number of interactions undergone by a mobile dislocation before being immobilized. Since the frequency of encountering obstacles in the friction regime in the direction of motion of the screw dislocation scales with $X = 2R^s + D$, X must thus replace $(\rho_{obs}^s)^{-0.5}$ in Eq. (19) and, given Eq. (11), it equals $(\rho_{obs}^s \lambda^s)^{-1}$.

With these two modifications, Eq. (19) becomes:

$$\frac{1}{\Lambda^s} = \left(1 - \frac{\tau_{eff}^s}{\tau_o}\right) \left(\frac{\sqrt{\alpha^{ss} \rho^s}}{K_{self}} + \frac{\alpha^s \lambda^s \rho_{obs}^s}{K_{obs}}\right). \quad (21)$$

Here again, at large temperature (low effective stress), λ^s tends to $1/\sqrt{\rho_{obs}^s}$ and Eq. (21) becomes similar to Eq. (19).

On the other hand, the coefficient y^s , which statistically corresponds to the average critical distance for screw dislocation annihilation by cross-slip [58], must be redefined within the present framework to account for the evolution of lattice friction with temperature. Within the drag regime, as the lattice friction is negligible, a reference critical annihilation distance noted y_{drag}^s is defined. The critical stress for dislocation annihilation τ_{drag} thus scales with $\mu b / (2\pi y_{drag}^s)$, which corresponds to the attraction between dislocations in a screw dipole. When the lattice friction is large, the dipolar attraction $\mu b / (2\pi y^s)$ must overcome the effective stress in addition to τ_{drag} . Consequently, the recovery coefficient can be estimated using the harmonic average:

$$\frac{1}{y^s} = \frac{1}{y_{drag}^s} + \frac{2\pi\tau_{eff}^s}{\mu b}. \quad (22)$$

As is physically intuitive, from Eq. (22) we see that at low temperature, a large friction stress induces a decrease in the annihilation distance, which results in a late dynamic recovery of the dislocation microstructure.

6. Finite-element simulations

In this section, the crystal plasticity model is now tested and the obtained results are compared with available data for pure iron single crystals. This comparison is restricted to the most robust available data reported in the literature, i.e. the temperature evolution of the critical resolved shear stress (CRSS) and the strain-induced lattice rotation. The finite-element (FE) method with finite strain formalism is adopted in order to reproduce realistic boundary conditions which are expected to play an important role in slip system activities.

6.1. Finite strain formulation

The set of constitutive equations previously presented is introduced into the FE simulation code CAST3M [60]. When large values of plastic strains are reached, they generally induce large rotations of the crystal as well, which

influence the projection of local stress on slip systems and eventually slip activity. In order to capture accurately such phenomena, a finite strain framework is used to implement the constitutive equations. We present in the following a summary of these equations.

The framework, first proposed in Ref. [61], decomposes the local transformation gradient \mathbf{F} into an elastic \mathbf{F}^e and a plastic \mathbf{F}^p gradients: $\mathbf{F} = \mathbf{F}^e \mathbf{F}^p$. The glide of all slip systems is represented by the \mathbf{F}^p transformation, while the rotation and elastic deformation of the crystal are described by \mathbf{F}^e . Following Ref. [62], the shear stress projected on a slip system s reads:

$$\tau^s = (\mathbf{F}^{eT} \mathbf{F}^e \mathbf{C} \mathbf{E}^e) : \mathbf{N}^s, \quad (23)$$

where \mathbf{C} is the fourth rank elasticity tensor, $\mathbf{E}^e = 1/2(\mathbf{F}^{eT} \mathbf{F}^e - \mathbf{I})$ is the Green–Lagrange elastic strain, and $\mathbf{N}^s = \mathbf{m}^s \otimes \mathbf{n}^s$ is the Schmid tensor with \mathbf{m}^s and \mathbf{n}^s the glide direction and the normal to the slip plane, respectively. For each time step of the FE simulation, one can first compute on each Gauss point of the structure the elastic part of the transformation provided the complete transformation and the plastic part of the transformation are known, $\mathbf{F}^e = \mathbf{F} \mathbf{F}^{p-1}$. In fact, \mathbf{F} is given by the FE code and \mathbf{F}^p is thus stored as an internal variable. The evolution equation of this tensor for each time step Δt reads [62]:

$$\Delta \mathbf{F}^p = \Delta \gamma^s \mathbf{N}^s \mathbf{F}^p, \quad (24)$$

where $\Delta \gamma^s$ is the increment of plastic slip on system s , calculated by integrating Eq. (6) over a time step, and considering the implicit summation rule on the superscript s .

Once \mathbf{F}^e is known, one can compute the resolved shear stress on each slip system using Eq. (23) and integrate all constitutive equations presented in the previous section. A Runge–Kutta (RK) explicit integration method with an adaptive step size to control the level of error, by combining a fourth-order RK and a third-order RK method, is used for this purpose in the following computations.

The crystal rotation can be eventually computed in a post-treatment procedure, which decomposes the elastic gradient into one symmetric tensor and one orthogonal tensor.

6.2. Geometry and simulation conditions

Two tensile specimen geometries are simulated, in order to investigate the role of boundary conditions (see Fig. 3). The first numerical study (called in the following the beam specimen) is a tensile test of a monocrystalline beam orientated in single slip. The beam, composed of $30 \times 2 \times 2$ cubic linear elements, is subjected to a tension in the initial longitudinal direction of the beam. The kinematic boundary conditions are imposed on the nodes of the extreme faces in the longitudinal direction. One of these faces is fixed while the nodes of the other face can only move by the same amplitude in the initial longitudinal direction of the beam. The crystallographic direction of the loading axis corresponds to the $[\bar{1}49]$ direction of the bcc crystal, which

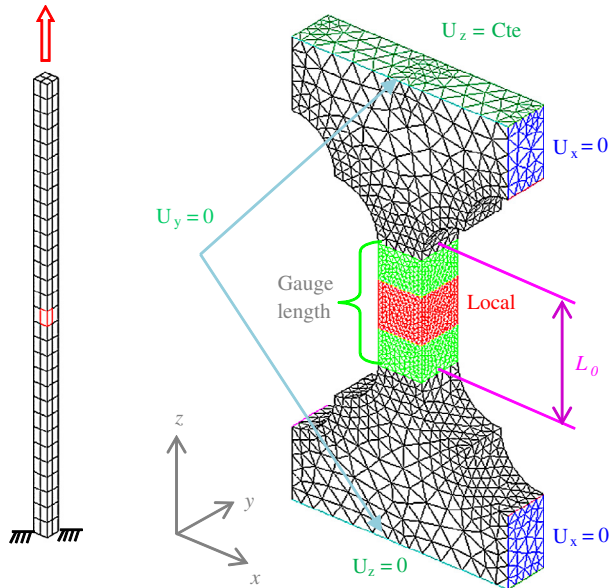


Fig. 3. The two meshes used to define the geometry of the beam and the flat tensile specimens used in the FE calculations.

Table 1
Values of the model parameters and material constants used in the FE simulations.

Parameter	Value	Parameter	Value
$\dot{\gamma}_0$ (rate constant)	10^{-6} s^{-1}	n (rate power)	50
ΔG_0	0.84 eV	τ_0	363 MPa
H	$2 \times 10^{11} \text{ s}^{-1}$	T_0	400 K
b (Burgers vector)	0.248 nm	k (Boltzmann constant)	$8.6 \times 10^{-5} \text{ eV K}^{-1}$
E (Young's modulus) in GPa	$236 - 0.0459T$	ν (Poisson ratio)	0.35
a^{ij} (noncollinear)	0.1	a^{ij} (collinear)	0.7
y_{drag} (dist. annihilation)	2 nm	ρ^s (primary system)	10^{12} m^{-2}
ρ^i (other systems)	10^{11} m^{-2}	$\dot{\epsilon}$ (applied strain rate)	10^{-4} s^{-1}
K_{self}	100	K_{obs}	33
Initial tensile axis	$[\bar{1}49]$		

is close to the center of the standard triangle of the stereographic projection, ensuring single slip conditions at the beginning of the test. The choice for such geometry and boundary conditions is justified in Ref. [63].

The second tensile specimen geometry considered for calculations (see Fig. 3) is a stiffer geometry representative of common tensile specimens (called the flat specimen). Simulation boundary conditions, also depicted in Fig. 3, are chosen in order to simulate experimental loading conditions. The orientation of the loading axis is the same as for the beam specimen. Comparison between both studies allows us to track the influence of the smaller length over the width ratio of the specimen geometry on the duration of the single slip stage and strain localization, coupled to thermal activation of plastic slip.

The values of all constants used in the calculations related to the proposed model are given in Table 1.

As already discussed in Section 2, one of the most important unknowns of the initial conditions is the dislocation microstructure formed at the end of stage 0 at different temperatures. As a starting point, we consider that in stage 0 only dislocation sources on the primary system were activated, leading to a large difference between dislocation density on this system compared to other systems. Thus in the simulations we take the initial dislocation density in the primary system to be 10 times larger than that in other systems (see Table 1). Note that we here simply assume isotropic elasticity, leading to the following expression for the shear modulus $\mu(T) = E(T)/(2(1 + \nu))$.

6.3. Results of the beam specimen

The field of plastic shear on the primary slip system is plotted in Fig. 4 on the final shape of the beam after 40% of conventional elongation and for different values of temperature. One can observe that the S-type shape is more pronounced in the intermediate regime of temperature where the activity of the primary slip system is the largest.

This result suggests that in this intermediate temperature regime, the secondary slip system is less active than at extreme values of temperature. This proposition is supported by Fig. 5 depicting the rotation of the loading direction in stereographic projection. At the beginning of all simulations, the tensile axis rotates, as expected from single slip conditions, from the center of the primary triangle towards the primary Burgers vector, which is the $[111]$ direction. At low and high temperatures, the tensile axis turns to the $[011]$ axis while crossing the $[001]$ – $[011]$ zone, separating the two stereographic triangles, which evidences the significant activity of the secondary slip system, since the combination of rotations towards $[111]$ and $[\bar{1}11]$ leads to a rotation towards $[011]$ direction. However, at intermediate temperature the loading axis crosses the $[001]$ – $[011]$ boundary and penetrates deep inside the secondary triangle, which indicates a large delay (overshoot) in the activation of the secondary system, though the resolved shear stress is higher on this slip system. The interpretation of this feature is tackled later in the discussion section.

The evolutions of the conventional shear stress and the principal variables of the model associated with the element located in the center of the beam are plotted in Fig. 6. In Fig. 6a, we show the evolution with deformation of the conventional shear stress, i.e. the normal applied stress multiplied by the initial value of the Schmid factor on the primary slip system. The thermal activation responsible for the decrease of yield stress with temperature is quite well reproduced in Fig. 6a. The hardening rate decreases also at low temperature. This result is in good agreement with existing experimental observations (see Section 7).

At 400 K, the local shear stress varies with the primary shear strain following a three-stage type curve (see Fig. 6b) contrary to curves obtained at lower temperatures. This

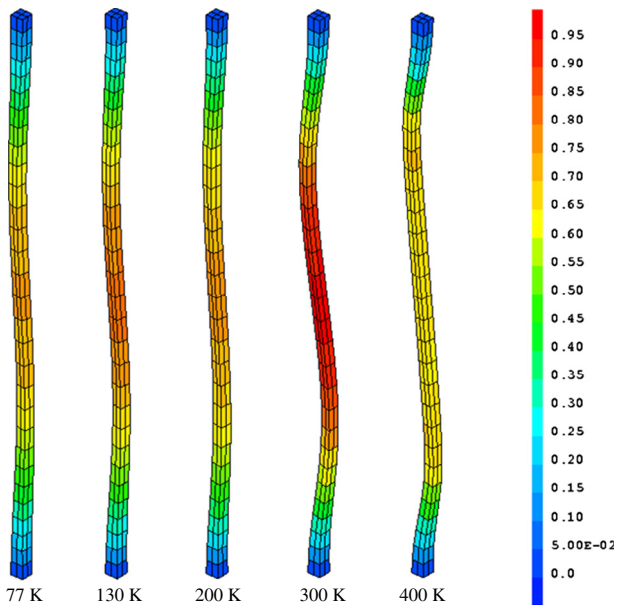


Fig. 4. Field of plastic shear on the primary slip system represented on the deformed beam after 40% of conventional elongation and for different temperatures.

change of regime is produced by the activation of the drag flow rule combined with a significant activation at the onset of stage II of the secondary slip system. At 200 K, an inflection point is also observed in Fig. 6b. It is not connected to the activation of the secondary system, but reflects the sharp transition occurring when the average length of screw segments reaches its critical value l_c (Fig. 6c) during the simulation, leading to the activation of the line tension component, as can be seen in Fig. 6e. Although this inflection is not desired, it is not considered to be important since it does not strongly affect the mechanical loading as seen in Fig. 6a.

In Fig. 6d, the evolution of the density of dislocation on the primary slip system is found to depend on temperature, and so on the evolution of the long-range stress (self-interaction) component shown in Fig. 6f.

At the highest temperature, the strong activation of the secondary slip system induces a rapid increase of the dislocation density on the primary slip system because the forest term in Eq. (21) results in large strain hardening.

6.4. Results of the flat specimen

The objective of this second set of calculations is to evaluate the influence of stiffer boundary conditions on the apparent mechanical behavior that can be deduced from the analysis of the evolution of the parameters of different CLs. Given the specimen geometry, the stress and strain tensors are strongly heterogeneous. Let F_z be the longitudinal component of the applied force. Experimental results are sometimes depicted using the conventional shear stress, i.e. $M_s F_z / S_o$, where M_s is the initial Schmid factor and S_o is the initial section of the deformed zone. In Fig. 7a the conventional shear stress is plotted as a function of the conventional shear strain, i.e. ε_{zz} / M_s . One can clearly see that the mechanical behavior deduced from average macroscopic data differs significantly from the actual material behavior in the deformation zone, depicted in Fig. 6. For this specimen, we define a “local zone” corresponding to a cube of height equal to the width of the sample and located in the center of the specimen “gauge length” defined in Fig. 3.

Detailed investigation of our results shows that the calculated mechanical behavior is sensitive to the region on which mechanical fields are averaged only at low temperature. Indeed, significant strain localization is observed only for temperatures lower than 200 K.

A three-stage hardening behavior is observed at 400 K, while the activity of the secondary slip shown in Fig. 7b does not correspond to an inflection point on the stress–strain curves at lower temperatures. For high and low temperatures, the end of stage I corresponds approximately to the crossing of the [001]–[011] zone, when the applied shear stress becomes larger on the secondary system than on the primary one. However, at intermediate temperature, namely 300 K, the activity of the secondary system is quite low, confirming the tendency noticed on the beam specimen (Fig. 5). The sharp decrease in the average length of screw segments with deformation and with temperature (Fig. 7c) leads to the appearance of the line tension component for $T > 200$ K, as can be seen in Fig. 7e, while the contribution of this component is zero at lower temperature. On the other hand, the self-interaction component is found to saturate for $T < 200$ K (Fig. 7f), which can be easily explained by the saturation of the primary density of dislocations for these temperatures (Fig. 7d).

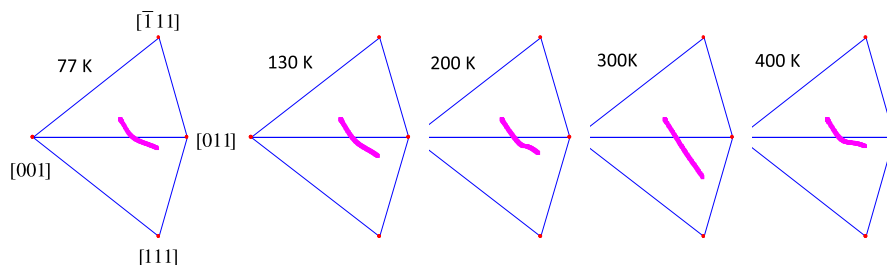


Fig. 5. Rotation of the loading axis in the stereographic projection as a function of temperature.

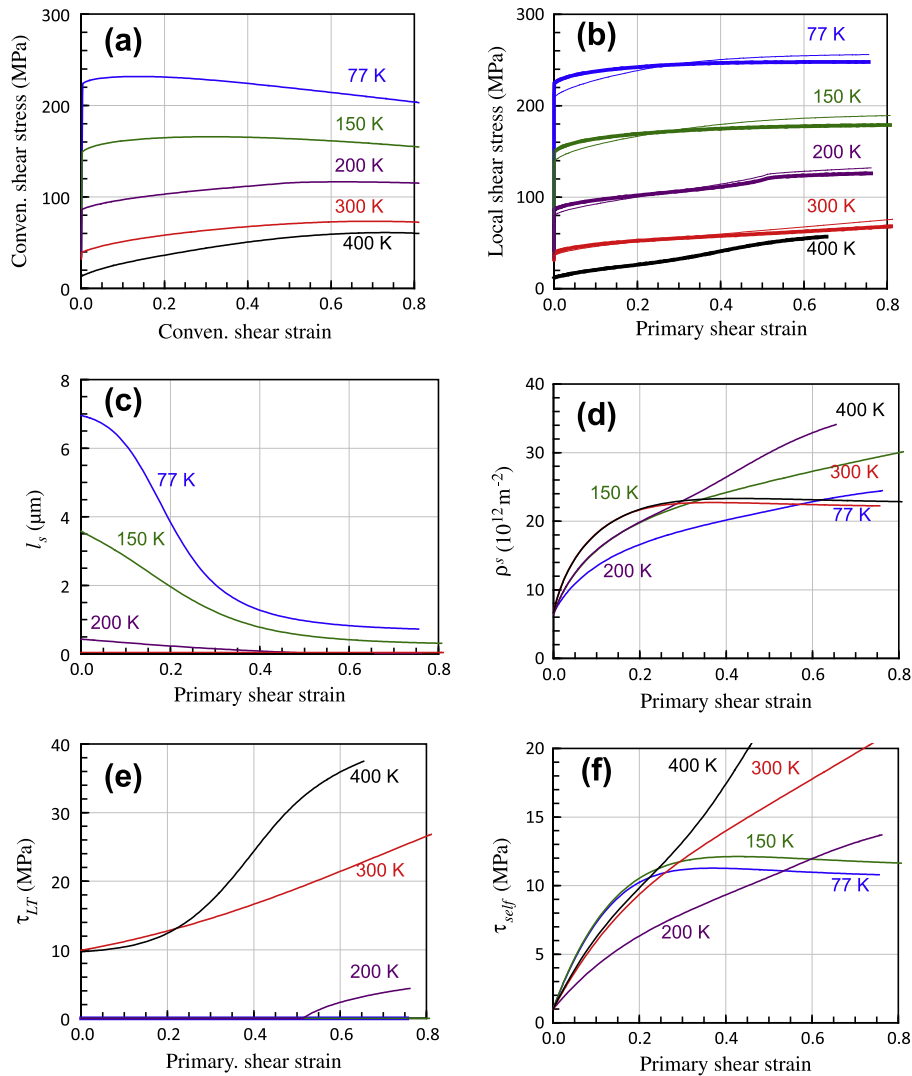


Fig. 6. Simulation results of the beam specimen: (a) conventional shear stress as a function of the conventional shear strain. Local evolutions as a function of plastic shear strain on the primary slip system of (b) shear stress on the primary (bold line) and secondary systems (thin line), (c) average length of screw dislocation segments (d) dislocation density on the primary slip system, (e) line tension and (f) the self components of the critical stress on the primary system.

Most of these results, and especially the ones at 300 K, do not differ significantly from those obtained on the beam specimen (Fig. 6). However, at low temperature, say $T < 200$ K, a significant and early apparent softening is observed on the flat specimen. This particular result is a direct consequence of strain localization, which is intense at 77 and 130 K, as observed in Fig. 8. In Fig. 8, we show also the map of the maximum shear stress. The heterogeneity of the latter is related to the stress localization, which enhances the local strain hardening and the decrease in the local section of the deforming zone. The strong heterogeneous field at low temperature indicates a strong necking, leading to the apparent softening observed in Fig. 7a.

7. Discussion and concluding remarks

In this paper we tried to translate recent results of DD simulations into constitutive equations governing plastic

deformation in bcc materials over wide range of temperature. The main improvement proposed here compared with other CLs reported in the literature is the consideration of non-screw dislocation curvature, which allows us to account for the temperature effect on dislocation interactions in two ways: (i) the interaction statistics is shown to obey a 1-D Poisson distribution; and (ii) the increase with temperature of the radius of curvature of non-screw segments leads to a smooth transition from a 1-D to a 2-D Poisson distribution of obstacle spacing, consistent with the classical square-root dependency on the dislocation density, known as the Taylor equation.

Although the transition from the friction to the drag regimes is guaranteed using a simple harmonic superposition rule, we are aware that a precise modeling of the transition regime requires much more attention to thermal activation details of the kink-pairs mechanism, such as the role of the annihilation and migration rates of kinks

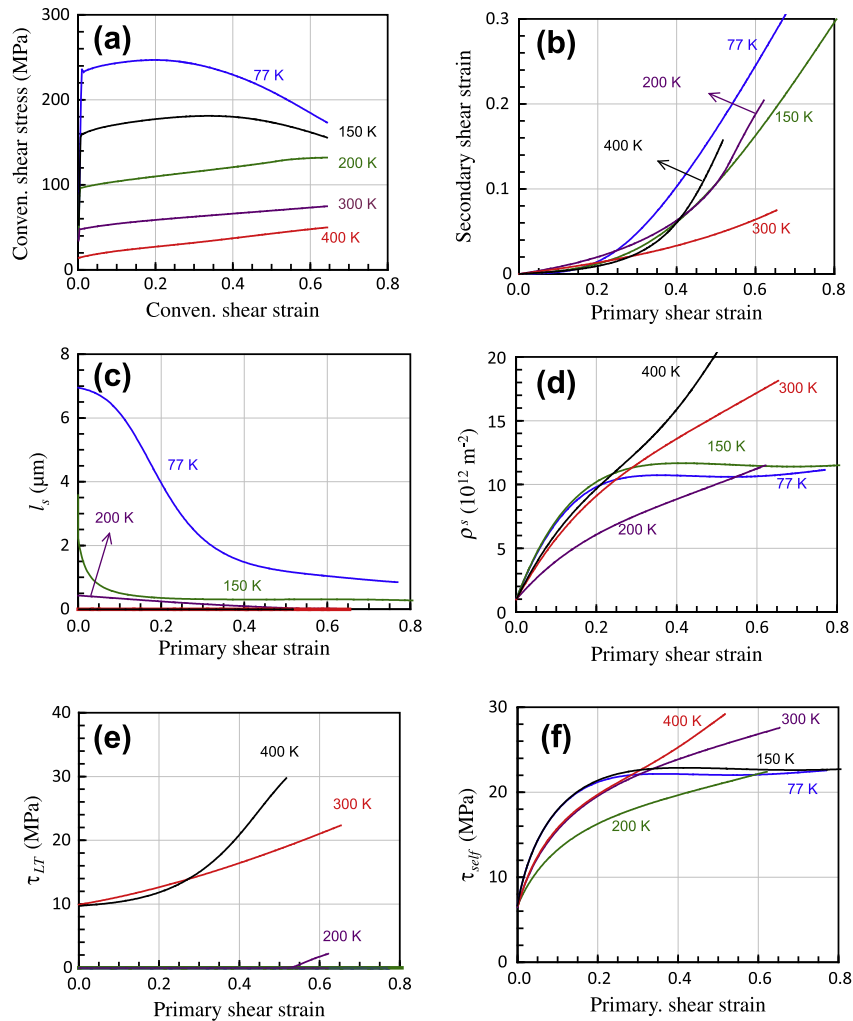


Fig. 7. Simulation results of a tension test on the flat specimen. (a) Conventional shear stress vs. conventional shear strain. Evolution as a function of the shear strain on the primary slip system of (b) the secondary shear strain, (c) the average length of screw segments, (d) the primary dislocation density, (e) the tension line and (f) the self components of the critical stress on the primary slip system.

(e.g. [64–66]). Also, at high temperature, the interaction with phonons can no longer be neglected [67] and the flow equation in the friction regime (Eq. (5)) must be modified in order to ensure the physically based transition to the drag viscous rate (Eq. (1)). However, we consider in this paper that the information at our disposal is insufficient to account quantitatively for this transition. We thus prefer the simple harmonic superposition law given in Eq. (6).

The predictions of the CL were tested with two tensile samples of different geometry. Comparison between Fig. 6 and Fig. 7 reveals the important following features: (i) the local crystallographic rotation and the yield stress are independent of the specimen geometry; (ii) the macroscopic hardening rate increases strongly with temperature; (iii) the strain localization appears earlier when the temperature decreases and when the width/length ratio of the specimen gauge increases; (iv) the extent of single slip is maximal at intermediate temperatures, including room temperature. At low temperatures, the effective stress is approximately equal to the resolved shear stress. The influence of the pre-exponential terms in Eq. (5) is thus reduced

and the secondary slip system activates as soon as its resolved shear stress becomes equal to that on the primary system. At high temperatures, the flow rule degenerates to Eq. (1) in which the critical stress $\tau_c^s = \sqrt{\tau_{self}^s{}^2 + \tau_{LT}^s{}^2}$ is identical for all slip systems due to the quadratic sum in τ_{self}^s and τ_{LT}^s . Consequently, secondary slip systems can be more easily activated, forcing the loading axis to rotate in parallel to the [111]–[011] boundary. The large extent of single slip at room temperature is therefore not an artifact of simulations. It was observed in experiments by Keh [68] and by Jaoul et al. [69]. We think our results provide a simple explanation for this a priori surprising feature. For a more general comparison with experimental results, we plot as a function of temperature in Fig. 9 the evolution of the CRSS computed from our simulations and the experimental values of the CRSS reported in the literature by Spitzig [49], Quesnel et al. [50] and Kuramoto et al. [51].

It can be clearly seen that the sensitivity of the CRSS to temperature is well reproduced by the FE simulations. Since the CRSS is not dependent on the specimen geometry, this agreement can be considered as a significant

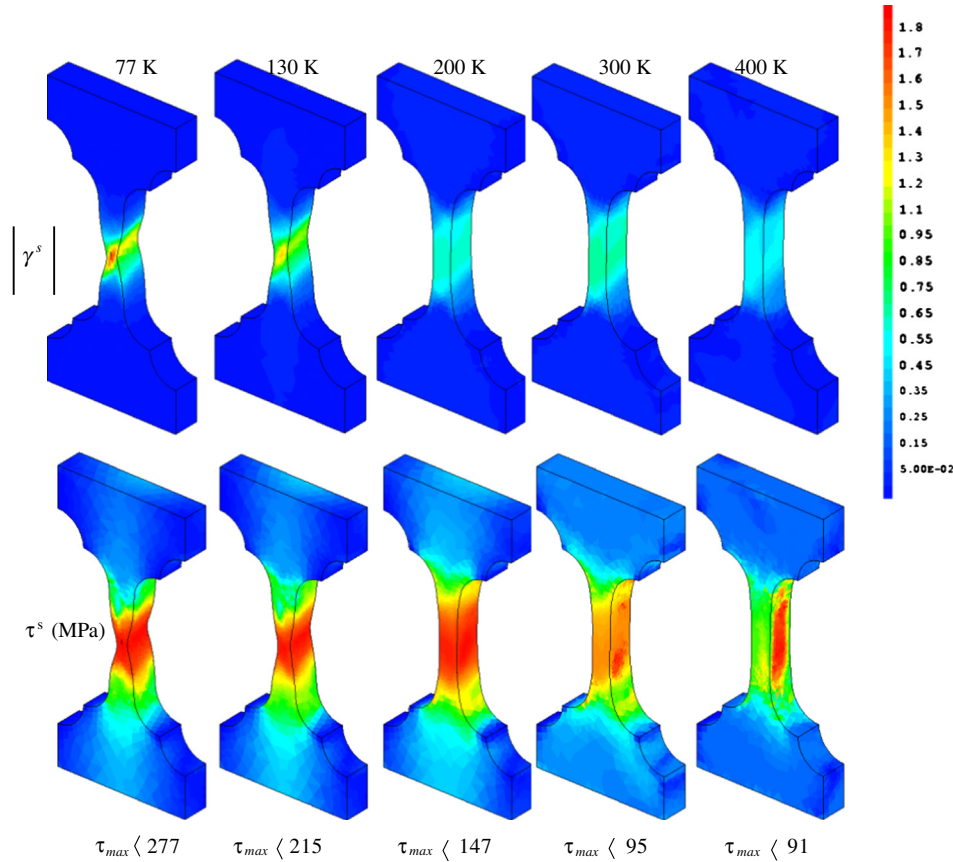


Fig. 8. Fields of plastic slip on the primary slip system and of maximum shear stress for different values of temperature and after a global elongation of 10% of the initial length of the sample.

validation of the CL proposed in this work. In Fig. 9, we show also the evolution of the effective stress and the critical stress as a function of temperature. As expected, the CRSS is close to the effective stress at low temperature and decreases strongly at high temperature. On the other hand, the critical stress, which is basically athermal in our model, is negligible at low temperature compared to the effective stress but becomes close to the applied stress at high temperature, say $T > 350$ K. This clearly underlines the transition between the low-temperature regime, controlled by the thermally activated screw dislocation motion, and the high-temperature regime, controlled by interactions with local obstacles and dislocation–dislocation interactions. A more detailed investigation of our results shows that the leading term in the harmonic mean in Eq. (6) for $T < 350$ K is the nucleation rate (Eq. (5)), while the drag rate (Eq. (1)) controls the total rate at higher temperatures. This feature is also in agreement with in situ transmission electron microscopy observations (e.g. [35]).

The last comparison that can be made with experiment is the shape of the stress–strain curves reported in the literature. However, such comparison is difficult since the experimentally reported curves exhibit many differences. For example, Kuramoto et al. [51] and Quesnel et al. [50] reported a set of flat curves with negligible hardening rate,

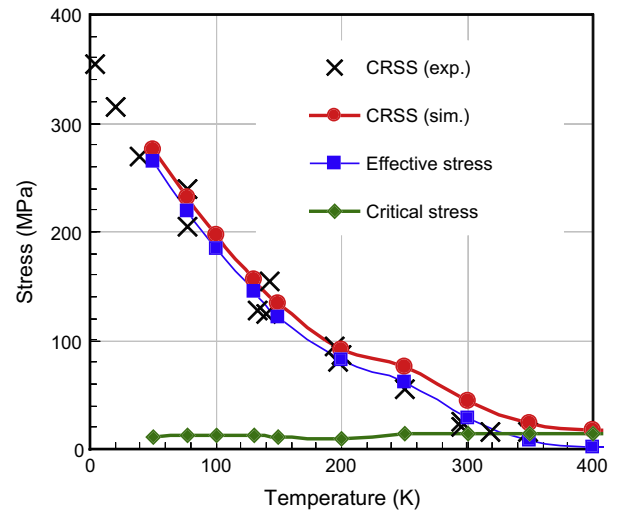


Fig. 9. Comparison between simulation and experimental results. The variation of the simulated effective stress and critical stress are also reported to highlight the duality between drag and friction regimes.

while Novak et al. [70] reported peaked curves at low temperatures and high hardening rate at high temperatures. We believe that these discrepancies are due to the difference in the chemical composition and the geometry of the tensile specimens used. Our results show an intermediate behavior

with pronounced tendency for strain localization (softening) at low temperatures and a high ratio of width/length ratio of the gauge zone.

To conclude, we propose in this paper a new set of equations for crystal plasticity modeling that allows for a phenomenological description of low-temperature plastic deformation in bcc materials, ensuring a smooth transition with the athermal regime known to prevail at high temperatures. A future step is the expansion of the present model to include grain boundary effects and non-monotonous loading.

Acknowledgment

This work is partially supported by the European project FP7 Project PERFORM60. Details on this project can be found on www.PERFORM60.net.

References

- [1] Peirce D, Asaro RJ, Needleman A. *Acta Metall* 1982;30:1087–119.
- [2] Roters F, Eisenlohr P, Hantcherli L, Tjahjanto D, Bieler T, Raabe D. *Acta Mater* 2010;58:1152–211.
- [3] Becker R. *Acta Metall Mater* 1991;39:1211–30.
- [4] Teodosiu C, Raphanel JL, Tabourot L. In: Teodosiu C, Raphanel JL, Sidoroff F, editors. *Large plastic deformations*. Rotterdam: A.A. Balkema; 1993. p. 153–68.
- [5] Fleck NA, Hutchinson JW. *Advances in applied mechanics*, vol. 33. New York: Academic Press; 1997. p. 1825–57.
- [6] Arsenlis A, Parks DM. *Acta Mater* 1999;47(5):1597–611.
- [7] Ma A, Roters F, Raabe D. *Acta Mater* 2006;54:2181–94.
- [8] Ma A, Roters F, Raabe D. *Int J Solids Struct* 2006;43:7287–303.
- [9] Kubin LP. *Rev Deform Behav Mater* 1976;1:243.
- [10] Christian JW. *Metall Trans A* 1983;14A:1237.
- [11] Louchet F, Kubin L. *Acta Metall* 1975;23:17.
- [12] Tome CN, Maudlin PJ, Lebensohn RA, Kaschner GC. *Acta Mater* 2001;49:3085.
- [13] Alankar A, Eisenlohr P, Raabe D. *Acta Mater* 2011;59:7003–9.
- [14] Stainier L, Cuitino AM, Ortiz M. *J Mech Phys Solids* 2002;50:1511–45.
- [15] Ma A, Roters F, Raabe D. *Comput Mater Sci* 2007;39:91–5.
- [16] Monnet G, Devincere B, Kubin LP. *Acta Mater* 2004;52:4317–28.
- [17] Tang L, Kubin LP, Canova GR. *Acta Mater* 1998;46:3221.
- [18] Tang M, Devincere B, Kubin L. *Model Simul Mater Sci Eng* 1999;7:893.
- [19] Naamane S, Monnet G, Devincere B. *Int J Plast* 2010;26:8.
- [20] Monnet G, Naamane S, Devincere B. *Acta Mater* 2011;59:451–61.
- [21] Queyreau S, Monnet G, Devincere B. *Int J Plast* 2009;25:361.
- [22] Thornton PR, Mitchell TE, Hirsch PB. *Philos Mag* 1962;7:337–58.
- [23] Nabarro FRN. *Strength of metals and alloys*. In: *Proc ICMSA 7*, vol. 3. Oxford: Pergamon Press; 1986. p. 1667–1700.
- [24] Sevillano G. In: Mughrabi, editor. *Plastic deformation and fracture of materials*, vol. 6. Weinheim: VCH Verlag; 1993. p. 19–88.
- [25] Rice JR. *J Mech Phys Solids* 1971;19:433.
- [26] Shanthraj P, Zikry MA. *Acta Mater* 2011;59:7695–702.
- [27] Franciosi P, Berveiller M, Zaoui A. *Acta Met* 1980;28:273–83.
- [28] Madec R, Kubin LP. In: Kitagawa H, Shibutani Y, editors. *IUTAM*. Dordrecht: Kluwer Academic Publishers; 2004. p. 69–78.
- [29] Brown N, Ekvall RA. *Acta Metall* 1962;10:1101–7.
- [30] Solomon HD, McMahon CJ. *Work hardening – metallurgical society*. In: *Conference*, vol. 46. New York: Gordon & Beach; 1966. p. 311–32.
- [31] Kubin LP, Louchet F. In: *Proc fifth int conf high voltage electron microscopy*, Kyoto; 1977.
- [32] Louchet F, Kubin LP. *Phys Stat Sol A* 1979;56:169.
- [33] Monnet G, Devincere B, Kubin LP. *Acta Mater* 2004;52:4317.
- [34] Tang M, Kubin LP, Canova GR. *Acta Mater* 1998;46:3221–35.
- [35] Caillard D. *Acta Mater* 2010;58:3493–503.
- [36] Hirth JP, Lothe L. *Theory of dislocations*. 2nd ed. New York: Wiley Interscience; 1982.
- [37] Schoeck G, Nabarro FRN. *Dislocations in solids*, vol. 2. Amsterdam: North Holland; 1980. p. 67.
- [38] Smidt FA. *Acta Metall* 1969;17:381–92.
- [39] Gilbert M, Queyreau S, Marian J. *Phys Rev B* 2011;84:174103.
- [40] Louchet F, Kubin LP, Vesely D. *Philos Mag A* 1979;39:433.
- [41] Ma A, Roters F, Raabe D. *Comput Mater Sci* 2007;39:91–5.
- [42] Queyreau S, Monnet G, Devincere B. *Acta Mater* 2010;58:5586.
- [43] Kocks UF. *Philos Mag* 1966;13:541.
- [44] Cuitino AM, Ortiz M. *Model Simul Mater Sci Eng* 1992;1:255–63.
- [45] Louchet F, Kubin L, Vesely D. *Philos Mag A* 1979;39:433.
- [46] Rauch EF. *Key Eng Mater* 1994;97–98:371.
- [47] Kinney JJ. *Probability—an introduction with statistical applications*. New York: John Wiley; 1997.
- [48] Van Kampen N. *Stochastic processes in physics and chemistry*. Amsterdam: North-Holland; 1992.
- [49] Spitzig WA. *Mater Sci Eng* 1973;12:191–202.
- [50] Quesnel DJ, Sato A, Meshii M. *Mater Sci Eng* 1975;18:199–208.
- [51] Kuramoto E, Aono Y, Kitajima K. *Scr Metall* 1979;13:1039–41.
- [52] Chomel P, Cottu JP. *Strength of metals and alloys*. In: *Fifth international conference 1979, Aachen*, vol. 2; 1979. p. 1013–18.
- [53] Kubin L, Louchet F. *Acta Metall* 1979;27:337–42.
- [54] Stein DF. *Acta Metall* 1966;14:99.
- [55] Taylor GI. *Proc Roy Soc* 1934;A145:362.
- [56] Kubin L, Devincere B, Hoc T. *Acta Mater* 2008;56:6040–9.
- [57] Kocks UF, Mecking H. *Prog Mater Sci* 2003;48:171–273.
- [58] Devincere B, Hoc T, Kubin L. *Science* 2008;320:1745.
- [59] Monnet G, Devincere B. *Philos Mag* 2006;86:1555–65.
- [60] <http://www-cast3m.cea.fr>.
- [61] Mandel J. *Plasticité classique et viscoplasticité*. CISM courses and lectures, vol. 97. Berlin: Springer Verlag; 1971.
- [62] Besson J, Cailletaud G, Chaboche JL, Forest S. *Mécanique non linéaire des matériaux*. Hermes; 2001.
- [63] Fivel M. *Etudes numériques à différentes échelles de la déformation plastique des monocristaux de structure CFC*. PhD thesis, INP Grenoble; 1997.
- [64] Dorn JE, Rjnak S. *Trans Metall Soc AIME* 1964;230:1052.
- [65] Guyot P, Dorn JE. *Can J Phys* 1967;45:983.
- [66] Hirth J, Lothe J. *Theory of dislocations*. Malabar (FL): Krieger; 1992.
- [67] Alshits VI, Indenbom VL. In: Nabarro FR, editor. *Dislocations in solids*, vol. 7. Amsterdam: North-Holland; 1986.
- [68] Keh AS. *Philos Mag* 1965;12:9.
- [69] Jaoul B, Crussard C. *Etude de la plasticité et application aux métaux*. Ecole des Mines de Paris; 2008.
- [70] Novak V, Sestak B. In: *4th Int conf strength of metals and alloys*, vol. 1; 1976. p. 156–60.